Journal of Applied Fluid Mechanics, Vol. 18, No. 2, pp. 374-388, 2025.
Available online at www.jafmonline.net, ISSN 1735-3572, EISSN 1735-3645.
https://doi.org/10.47176/jafm.18.2.2816

Large Eddy Simulation of Swirl Topology Evolution in Strong Oxidant Jet Milling Force Field

Y. Yu[1,2], K. Chen[3], D. Wang[1,4], Y. Qin[1,4] and J. Liu[1,4†]

[1] *National Special Superfine Powder Engineering Research Center of China, Nanjing 210094, Jiangsu, China*
[2] *Sino-France Engineering School, Nanjing University of Science and Technology, Nanjing 210094, Jiangsu, China*
[3] *School of Energy and Power Engineering, Nanjing University of Science and Technology, Nanjing 210094, Jiangsu, China*
[4] *School of Chemical Engineering, Nanjing University of Science and Technology, Nanjing 210094, Jiangsu, China*

†Corresponding Author Email: jie_liu_njust@126.com

ABSTRACT

In this paper, Large Eddy Simulation (LES) is employed to investigate the evolution characteristics of a spiral jet mill. This study aims to provide a theoretical reference for the numerical simulation and design optimization of spiral jet mills. To evaluate the influence of grids on simulation accuracy, grid convergence index (GCI) analysis was carried out on three sets of non-structural grids with equal proportion refinement. The visualization results demonstrate that the feeding gas traction and jet impact attenuation contribute to momentum conversion from the edge to the central domain, facilitating the development of the central swirl. The cross-scale chamber structure makes the turbulent coherent structure in the swirl evolution tend to be complex and disordered. A large-scale annular swirl is formed by stacking and winding multiple strip vortices. By comparing with the steady-state solution calculated using the k-epsilon model, it is confirmed that the aerodynamic characteristics in the micronization chamber stabilize at 400 ms. At this time, the combined action of the radial and tangential velocity forms a spiral airflow trajectory.

Article History

Received May 2, 2024
Revised August 25, 2024
Accepted August 29, 2024
Available online December 4, 2024

Keywords:

Swirl topology
Flow characteristic
Heat transfer
Coherence vortex
Large eddy simulation

1. INTRODUCTION

Composite solid propellant is a heterogeneous material with a high solid loading, consisting of discrete particles such as strong oxidizers and highly reactive metal fuels dispersed within an adhesive matrix. Currently, jet mills are widely employed for the preparation of high-purity oxidizers. Compared to other types of jet milling equipment—such as target, spray, and fluidized bed mills—the high-energy shear movement of the jet and particles in a spiral jet mill operates without mechanical components. This design effectively mitigates the risk of powder contamination (Scott et al., 2021c). To meet the demand for multi-scale ammonium perchlorate (AP) particle sizes (Gross & Beckstead, 2010; Isert et al., 2016; Bojko et al., 2020; Chen et al., 2023), our team has independently developed spiral jet milling technology for batch preparation of sub-micron and nano-scale strong oxidants. These strong oxidants exhibit excellent thermal decomposition performance and pose a deflagration risk in pressure environments above 2 MPa, necessitating higher safety requirements for the jet milling process (Nagendra et al., 2019).

Figure 1 illustrates the operational principle of the spiral jet mill. High-speed gas (typically dry air or nitrogen) enters the micronization chamber through the inlet pipe and the working medium distribution chamber. The gas forms a swirl gradient field that attenuates radially from the center to the wall. The fluid drag force drives the feed particles toward the wall surface of the micronization chamber, resulting in high-energy collisions between particles and between particles and the wall (Sabia et al., 2022). The drag and centrifugal forces imposed by the swirling flow field define the radial position of multi-scale particles through the aerodynamic classification mechanism (refer to Fig. 2) (Tanaka & Yanse 2008; Luczak et al., 2019; Sabia et al., 2021). When the radial bed shears each other, high-energy collisions cause stress concentration inside the particles and induce crack growth.

NOMENCLATURE

$C_{1\varepsilon}$	model constants	Re	Reynolds number
$C_{2\varepsilon}$	model constants	$\bar{S}_{ij}$	strain rate tensor
$C_{3\varepsilon}$	model constants	t	time
Nu	Nusselt number	T	temperature
p	pressure	τ_{ij}	subgrid scale stresses
ρ	fluid density	$\bar{u}_i, \bar{u}_j$	resolved velocity in *i* and *j* direction, *i*, *j*=1, 2, and 3
λ	diffusion coefficient for energy transport	μ_t	turbulent viscosity
ε	turbulent kinetic energy dissipation rate	v	velocity
k	turbulent kinetic energy	v_t^p	tangential velocity of particles
σ_ε	turbulent Prandtl number for ε	v_t^f	tangential velocity of fluid
G_b	generation of k	v_r^p	radial velocity of particles
G_k	generation of turbulent kinetic energy due to mean velocity gradients	v_r^f	radial velocity of fluid
σ_k	turbulent Prandtl number for k	Y_M	fluctuation caused by turbulent transition expansion
D	the radius of the micronization chamber	l	characteristic length
U	velocity scale	L	length scale

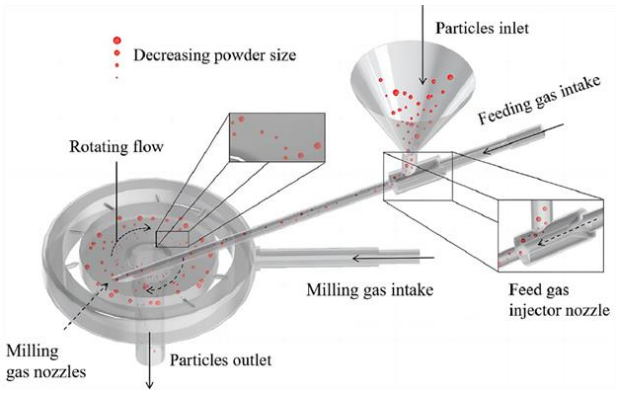

Fig. 1 Working principle and system schematic of spiral jet mill

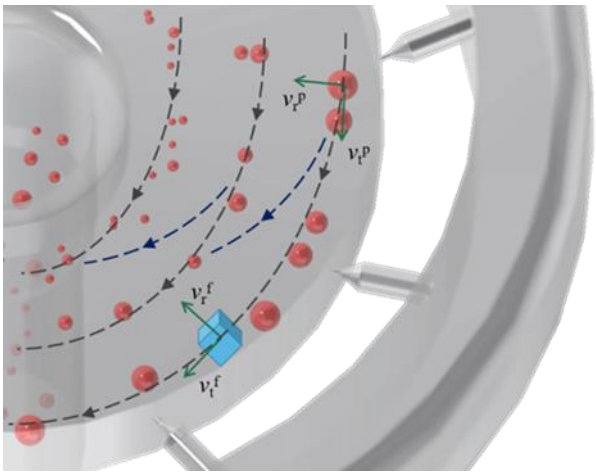

Fig. 2 Velocity components in the Eulerian description of the milling fluid and particle motion. Green arrows labelled v_t (tangential velocity) and v_r (radial velocity) are used to describe the velocity components of particles and fluid micro-elements, respectively

The particle structure is refined to a micron-scale by high strain (Scott et al., 2021a).

Currently, the design criteria for efficient mills primarily rely on experience-driven experimental activities. However, the presence of sensors can disrupt the swirling flows within the micronization chamber, and the high-energy collisions of dense-phase particles may reduce probe sensitivity (Sabia et al., 2022). There are considerable technical limitations in dynamically characterizing thermodynamics, fluid dynamics, and particle size scales within the spiral jet mill. Nevertheless, advancements in computational capabilities have made it possible to utilize numerical simulation tools to effectively investigate the interactions between the milling force field and dense-phase particle abilities (Silvester et al., 2007; Rajeswari et al., 2011; Rodnianski et al., 2013; Brosh et al., 2014; Bnà et al., 2020; Scott et al., 2021b).

Rajeswari et al. (2011) developed a three-dimensional Computational Fluid Dynamics (CFD) model to comprehensively investigate the flow dynamics of the gas-solid phase during the fine milling process. Bnà et al. (2020) assessed the collision frequency and energy dissipation of multi-scale particles by describing the steady-state eddy current gradient within the jet mill. They utilized the Eulerian method to characterize this gradient, tracing all particles in the computational domain using the Lagrange equation. Building on the CFD-DEM one-way coupling model, they introduced the concept of capturing the damping effect of dense particles on the flow field within a high-order coupling system. Scott et al. (2021b) Scott2021bemployed the CFD-DEM four-way coupling method to analyze the retention effect of a radially moving granular bed under a centrifugal field, as well as the influence of related dynamics on the particle-fluid flow field and collision energy dissipation. The numerical simulation results indicated that a high-quality solid-phase load reduces the impact velocity of the particles, thereby preventing them from being ejected at high speed into the central phase of the micronization chamber.

As illustrated in Fig. 2, particle breakage in the micronization chamber occurs spontaneously, driven by a high-speed vortex. The balance of inertial forces acting on particles of varying sizes depends on the evolution of radial and tangential velocities. Numerous researchers have conducted numerical simulations of particle dynamics during milling processes to enhance the understanding and manipulation of the grinding effects in spiral jet mills. Based on the velocity flow field simulated using single-phase fluid dynamics, Rodnianski et al. (2013) identified the particle cutting size that characterizes the classification phenomenon. The particle classification equation is defined by gas velocity, particle velocity, and jet mill dimensions, making it suitable for predicting dilute phase flow. In a separate study, Brosh et al. (2014) employed a coupled CFD-DEM code to monitor the motion of the particle phase during mill operation. They calibrated an empirical crushing function to predict the fatigue fracture behavior of particles during impact events. However, due to limitations in hardware and time, their model remained in the experimental stage.

Wu and Squires (2000) applied large eddy simulation (LES) to study the three-dimensional turbulent boundary layer on a rotating disk for the first time. Their results confirmed that the injection mechanism promotes the generation of shear stress. Wu et al. (2019) employed unsteady Reynolds-averaged Navier–Stokes (RANS) and LES turbulence models to investigate the hydrodynamic behavior of fluid oscillators and unsteady jets. Séverac et al. (2007) used the LES method to study the turbulent flow in a closed rotor-stator micronization chamber. They used the spectral vanishing viscosity method to achieve the condition $Re = 10^6$. The finite chamber effect shows that the main characteristics of turbulence are related to the radial direction. In the flow region with the weakest turbulence level, the Q criterion shows a spiral structure associated with crossflow instability. In the fully turbulent flow region, the structure becomes finer and aligned along the tangential direction.

The LES model decomposes turbulence into the direct numerical simulation of large-scale structures and parameterized simulation of small-scale structures. In the spiral jet milling process, both large-scale vortices formed by jet merging and small-scale turbulence from unmerged jets coexist. By simulating subgrid-scale turbulence through LES, it is possible to describe the fluid dynamic behavior of high Reynolds number jets in the micronization chamber more accurately. Low Reynolds number flow is typically dominated by viscous forces, resulting in relatively stable fluid motion where the formation of turbulent vortices is uncommon. In such cases, the LES model may struggle to capture large-scale structures in the flow. LES has unique advantages in describing high Reynolds number jets and multi-scale swirl structures, which provides a sufficient theoretical basis for studying the flow field evolution mechanism of the spiral jet mill.

The swirl evolution process reflects the stability of the milling force field. In this study, we employ the LES method to investigate the dynamic behavior of gas flow within the chamber of a spiral jet mill. The flow field in the micronization chamber is complex, and the high Reynolds number jet and the sub-scale vortex exist simultaneously. The wall-adapting local eddy-viscosity (WALE) model closes the turbulence governing equation on the subgrid scale. Grid Convergence Index (GCI) analysis is conducted to ensure grid independence and establish confidence in the LES solution results. This study mainly demonstrates the process of jet expansion and fusion in the micronization chamber to form a swirling topology. The analysis is carried out from the aspects of the velocity field, component velocity, temperature distribution, and coherent structure.

2. GOVERNING EQUATIONS AND NUMERICAL METHODS

In this study, LES and k-epsilon models are used to describe the unsteady and steady-state conditions of high Reynolds number turbulence in the computational domain.

2.1 Large Eddy Simulation Equations

The large-scale turbulence in the computational domain of the LES model is controlled by three-dimensional unsteady Navier–Stokes equations and energy equations. By filtering the Navier–Stokes equations in the Fourier space, the dynamic range of the analytical turbulence scale in the computational domain is reduced (Chen et al., 2021).

$$\frac{\partial \rho}{\partial t} + \frac{\partial}{\partial x_i}(\rho \bar{u}_i) = 0 \tag{1}$$

$$\frac{\partial}{\partial t}(\rho \bar{u}_i) + \frac{\partial}{\partial x_i}\left(\rho \bar{u}_i \bar{u}_j\right) = \frac{\partial}{\partial x_j}(\sigma_{ij}) - \frac{\partial \bar{p}}{\partial x_j} - \frac{\partial \tau_{ij}}{\partial x_j}$$

$$\frac{\partial(\rho \bar{h})}{\partial t} + \frac{\partial}{\partial x_i}\left(\rho \bar{u}_i \bar{h}\right) - \frac{\partial \bar{p}}{\partial t} - \bar{u}_j \frac{\partial \bar{p}}{\partial t} - \frac{\partial}{\partial x_j}\left(\lambda \frac{\partial \bar{T}}{\partial x_i}\right) \tag{2}$$

$$= \frac{\partial}{\partial x_j}\left[\underbrace{\rho\left(\overline{u_i h} - \bar{u}_i \bar{h}\right)}_{subgrid\ enthalpy\ flux}\right] \tag{3}$$

Although the inertial sub-scale vortex generated by the cascade of turbulent energy is smaller than the grid size, it does not diminish the dynamic significance of turbulence (Jafari et al., 2008). The motion of large-scale eddies is influenced by the nonlinear coupling effects of the sub-scales. To effectively close the large-scale turbulence governing equations at the subgrid level, an explicit physical model must be employed to replace the subgrid stress tensor (Wang et al., 2023). Based on the Boussinesq hypothesis, the subgrid-scale stress is defined as follows:

$$\tau_{ij} \equiv \rho \overline{u_i u_j} - \rho \bar{u}_i \bar{u}_j \tag{4}$$

The eddy current-viscosity model expression of subgrid-scale tensor is applied to τ_{ij},

$$\tau_{ij} - \frac{1}{3}\tau_{kk}\delta_{ij} = -2\mu_t \bar{S}_{ij} \tag{5}$$

The vortex-viscosity model assumes τ_{ij} is proportional to the strain rate tensor $\bar{S}_{ij}$ of the filtration field. The subgrid-scale turbulent viscosity μ_t is closed by the WALE model.

$$\bar{S}_{ij} = \frac{1}{2}\left(\frac{\partial \bar{u}_i}{\partial x_j} + \frac{\partial \bar{u}_j}{\partial x_i}\right) \quad (6)$$

$$\mu_t = \rho L_s^2 \frac{(S_{ij}^d S_{ij}^d)^{3/2}}{(\bar{S}_{ij}\bar{S}_{ij})^{5/2} + (S_{ij}^d S_{ij}^d)^{5/4}} \quad (7)$$

$$S_{ij}^d = \frac{1}{2}\left(\bar{g}_{ij}^2 + \bar{g}_{ji}^2\right) - \frac{1}{3}\delta_{ij}\bar{g}_{kk}^2 \quad (8)$$

$$\bar{g}_{ij} = \frac{\partial \bar{u}_i}{\partial x_j} \quad (9)$$

$$L_s = \min\left(kd, C_w V^{\frac{1}{3}}\right) \quad (10)$$

Based on the dynamic calibration of eddy current at high gradient attenuation of velocity by temperature, C_{wale} adopts the default viscosity constant 0.325 of Sutherland formulas. Compared with the Smagorinsky model, the WALE model combines the C_{wale} constant to reproduce the transition behavior from laminar to turbulent flow at the wall boundary (Alzwayi et al., 2014).

2.2 k–Epsilon Equations

The fluid grinding force field has transitioned from laminar to turbulent flow while evolving toward dynamic equilibrium. Thus, we can conclude that the flow field in the steady-state computational domain is entirely turbulent. Solving Reynolds-Averaged Navier-Stokes (RANS) equations can calculate the steady-state flow field of the spiral jet mill (Kumar & Jackson, 2021):

$$\frac{\partial \bar{u}_m}{\partial t} + \bar{u}_p \frac{\partial \bar{u}_m}{\partial x_p} = -\frac{1}{\rho}\frac{\partial p}{\partial x_m} + \frac{\partial}{\partial x_p} + \left((v + v_t)\frac{\partial \bar{u}_m}{\partial x_p}\right) + g_m \quad (11)$$

Including, $\bar{u}_m$ is the Reynolds-averaged velocity component.

Transport equation for turbulent kinetic energy (k):

$$\frac{\partial}{\partial t}(\rho k) + \frac{\partial}{\partial x_i}(\rho k u_i) = \frac{\partial}{\partial x_j}\left[\left(\mu + \frac{\mu_t}{\sigma_k}\right)\frac{\partial k}{\partial x_j}\right] + G_k + G_b - \rho\varepsilon - Y_M + S_k \quad (12)$$

And equation for dissipation of turbulent kinetic energy (ε):

$$\frac{\partial}{\partial t}(\rho\varepsilon) + \frac{\partial}{\partial x_i}(\rho\varepsilon u_i) = \frac{\partial}{\partial x_j}\left[\left(\mu + \frac{\mu_t}{\sigma_\varepsilon}\right)\frac{\partial \varepsilon}{\partial x_j}\right] + C_{1\varepsilon}\frac{\varepsilon}{k}(G_k + G_{3\varepsilon}G_b) - C_{2\varepsilon}\rho\frac{\varepsilon^2}{k} + S_\varepsilon \quad (13)$$

Where k is the turbulent kinetic energy, ε is the turbulent kinetic energy dissipation rate, and μ_t is the turbulent viscosity. σ_k and σ_ε are the turbulent Prandtl numbers for k and ε respectively. G_k represents the generation of turbulent kinetic energy due to mean velocity gradients while G_k is the generation of k. Y_M is the fluctuation caused by turbulent transition expansion, $C_{1\varepsilon}$, $C_{2\varepsilon}$ and $C_{3\varepsilon}$ are model constants.

2.3 Modeling and Experiments

The fluid calculation domain for the GQF-3 jet mill is established by simplifying its shell based on CAD drawings provided by Nanjing University of Science and Technology. As illustrated in Fig. 3, compressed air is introduced into the venturi ejector through the intake pipe. This jet creates a vacuum gradient in the adsorption chamber, effectively capturing the feed particles and directing them into the micronization chamber. The upper cover and the seat ring are secured in place with fastening screws. The seat and the inner milling ring form the working medium distribution chamber through mechanical constraints. The inner milling ring features ten nozzles arranged in a tangential configuration at equal angles. The A-A section represents the intersection plane of the inlet pipe axis and the hopper axis, while the B-B

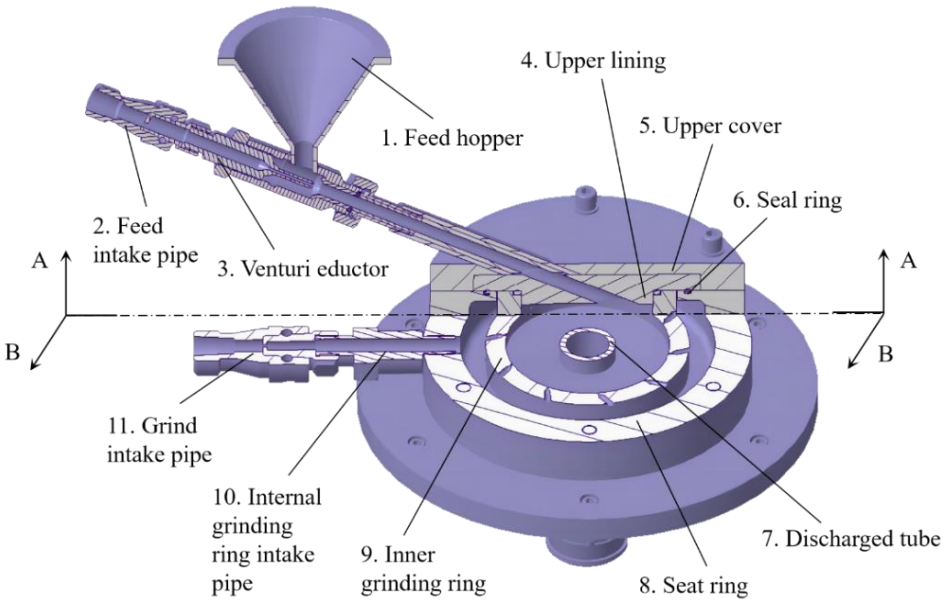

Fig. 3 In-house made CAD drawing of GQF-3 jet mill

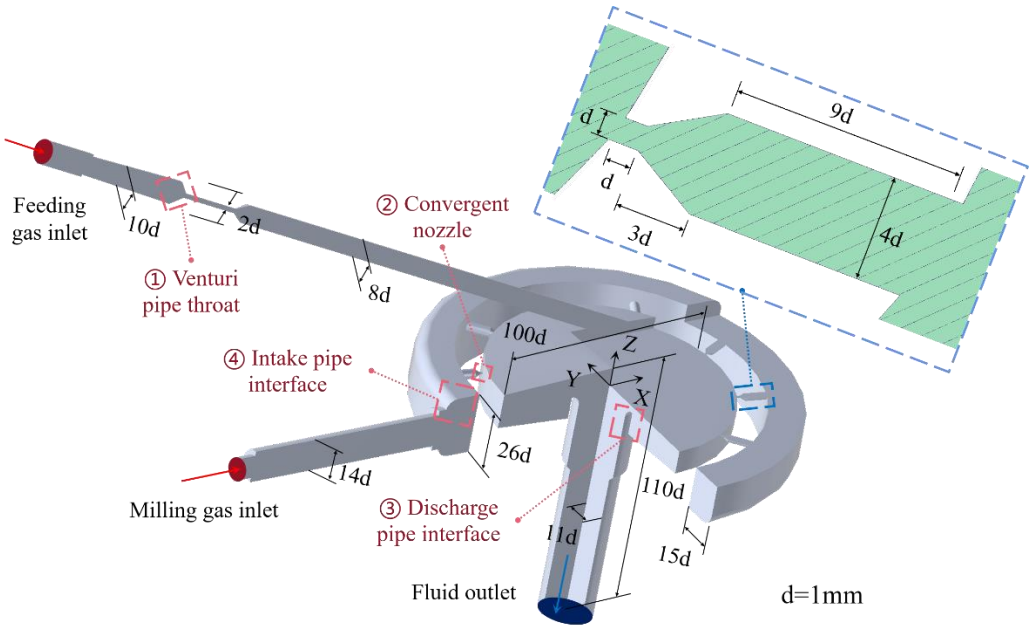

Fig. 4 Sketch of computational domain cross-section

Table 1 Typical operational conditions for a pilot-scale jet mill (Bnà et al., 2020)

Feeding pressure (MPa)	Milling pressure (MPa)	Upstream temperature (℃)	Downstream temperature (℃)	Feeding flow rate (Nm^3/h)	Milling flow rate (Nm^3/h)
0.6±0.005	0.55±0.005	23	31.5	8.5±1	20.5±1
0.7±0.005	0.65±0.005	23	34.2	9.5±1	26.5±1
0.8±0.005	0.75±0.005	24	38.7	10.5±1	30.0±1
0.9±0.005	0.85±0.005	23	39.3	11.5±1	36.2±1
1.0±0.005	0.95±0.005	22	42.2	12.5±1	41.1±1

section represents the intersecting plane of the axis of the inner grinding ring nozzle. AP particles are not added to the LES transient flow field evolution process. Therefore, the computational domain of the hopper above the venturi injector is suppressed by physics. Figure 4 provides detailed information about the cross-section of the computational domain, the configuration of the nozzles, and the boundary conditions.

In spiral jet milling, measurements are typically taken where gas flow is controlled, such as near regulation valves and discharge points. However, it is challenging to place a probe inside the micronization chamber to monitor pressure, temperature, or flow rates during the process, as its presence could disrupt the normal flow path of the milling gas. Gauge pressure, temperature, and flow rate data were collected during actual jet mill operations (see Table 1). The mass flow was calculated to establish the local inlet boundary conditions. The following assumptions were made when selecting the solver and boundary conditions:

- Turbulent flow: Given the high Reynolds numbers expected, the turbulent nature of the milling fluid flow cannot be neglected;

- Adiabatic flow: Considering minor thermal exchange effects due to the rapid variations in flow properties;

- Compressible ideal gas: Given the high Mach numbers expected, the compressible nature of the milling fluid must be considered;

- Constant dynamic viscosity of fluid: Large turbulent eddies interact with and extract energy from the mean flow through a process called vortex stretching. The characteristic velocity v and characteristic length l of the larger eddies are similar to the velocity scale U and length scale L of the mean flow. Hence, a 'large eddy' Reynolds number $Re_l = vl/\nu$ formed by combining these eddy scales with the dynamic viscosity, will be large in all turbulent flows, as it is not significantly different in magnitude from UL/ν. This suggests that the large eddies are dominated by inertia effects and that viscous effects are negligible (Versteeg & Malalasekera 1995). In addition, turbulence involves complex interactions among vortices of multiple scales. The presence of numerous irregular fluid structures leads to increased energy dissipation, making the transfer of energy and momentum more effective. This enhanced momentum transfer mechanism results in turbulent viscosity being significantly higher than molecular viscosity. Therefore, assuming the dynamic viscosity of the gas flow remains constant, its variation's impact on large eddies is neglected.

In these assumptions, the mass flow rate can be evaluated from nozzles chocking conditions, i.e., by the

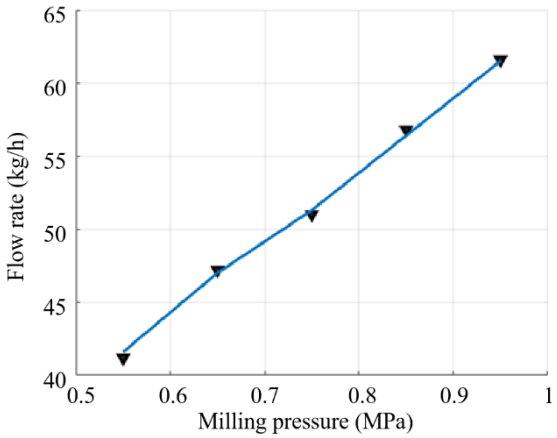

Fig. 5 Mass flow rate as a function of milling pressure: comparison between the experimental measurements and calculated values

Table 2 Fluid properties & boundary condition

Parameters	Value
Density (formulation) (kg/m^3)	Ideal gas law
Constant pressure specific heat (J/kg K)	1006.43
Thermal conductivity (W/m K)	0.02
Heat flux on the wall (W/m^2)	0
Dynamic viscosity (Pa s)	1.79E-05
Molecular weight (g/mol)	28.01
Specific heats ratio	1.4
Feeding pressure (MPa)	0.8
Milling pressure (MPa)	0.75
Pressure at the outlet (MPa)	0.101

following expression:

$$\dot{m} = p_0 A_t \left[\frac{k}{RT_0} \left(\frac{2}{k+1} \right)^{\frac{k+1}{k-1}} \right]^{\frac{1}{2}} \tag{14}$$

The mass flow is controlled by the throat area of the nozzles A_t and the total upstream quantities T_0 and p_0. The fluid at inlets is assumed to be at the stagnation temperature T_0. The gas characteristics also play a role through the values k (heat capacity ratio) and R (gas constant). In this work, the carrier phase is air, and no other gases were accounted for. The solution of Eq. (14) gives the mass flow rate passing through each grinding nozzle, and this value can be used to calculate the milling mass flow rate and compare it with the measured value as a consistency check.

Figure 5 presents the experimental milling flow rate and the calculated flow rate for various milling pressures. There is a slight discrepancy between the actual and simulated geometries. This difference, which may account for the imperfect match between the two flow rate values, remains within an acceptable margin of 2% for the current calculations. Due to the neglect of heat exchange between the gas flow and the wall, the fluid domain wall is a non-slip adiabatic boundary. The inlets for both the feeding gas flow and the milling gas flow, along with the outlet for the gas flow, are defined as pressure boundaries. During the initialization stage of the simulation, the boundary surface ressure is atmospheric. Detailed parameters about the boundary settings and the distinctive characteristics of the gas flow are in Table 2.

3. COMPUTATIONAL GRID CONSTRUCTION AND MESH SENSITIVITY ANALYSIS

To accurately represent the dynamic fluid flow within the computational domain, we conducted a study to ensure grid independence. For high Reynolds number flows with thin boundary layers, it is essential to economize computing resources by graded non-uniform meshes. By adjusting the minimum size of the surface mesh, we obtained three different mesh configurations: 0.215 million elements (coarse grid), 0.615 million elements (medium grid), and 1.818 million elements (fine grid). Figure 6 illustrates the details of the medium grid on the nozzle-cutting plane. The stretching factor of the mesh in the normal direction to the wall is 1.2. The height of the wall-normal direction of the first layer grid is $\Delta y = 0.0005D$ (D is the radius of the micronization chamber), and the corresponding y+ is about 15. Through grid time step dependence, we can evaluate the robustness and accuracy of numerical simulation in capturing the flow characteristics.

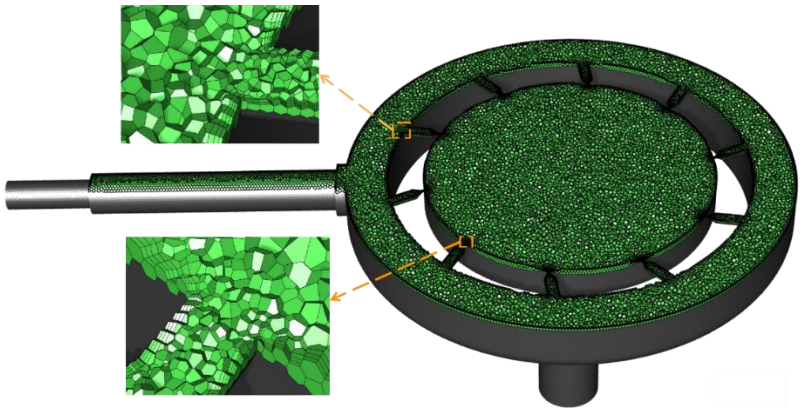

Fig. 6 Medium grid details

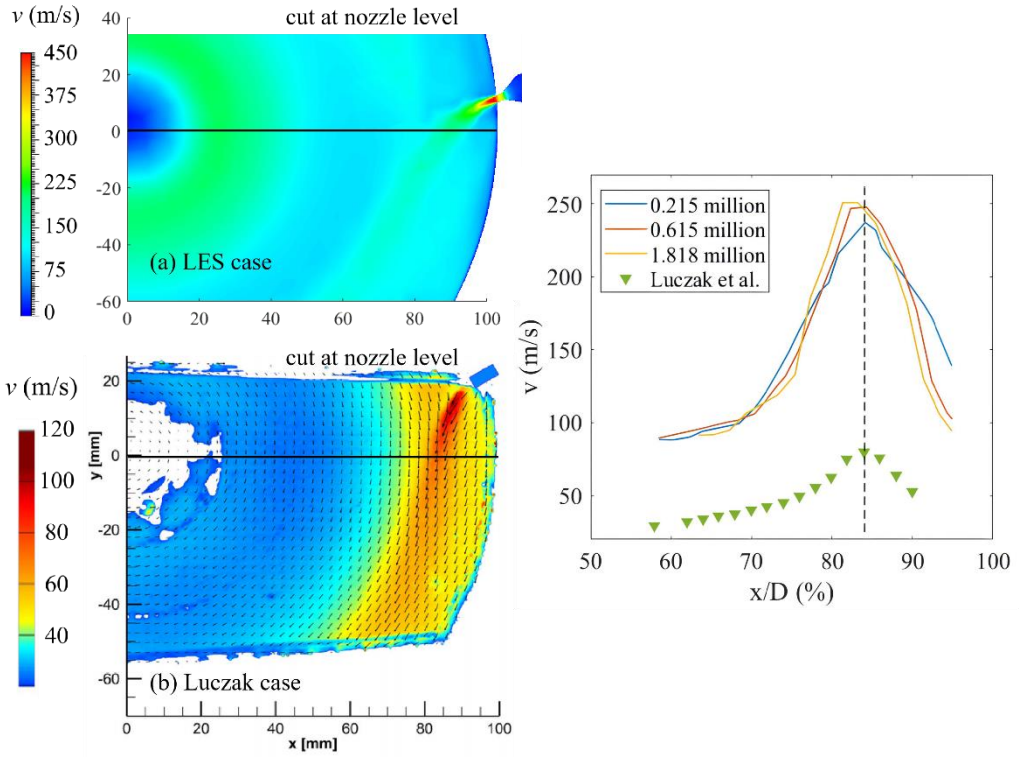

Fig. 7 Grid independence for LES and Luczak case at the length y = 0 mm. (a) LES case: 214916 grids, eight nozzles, milling gas pressure is 0.75 MPa. (b) Luczak case: eight nozzles, milling gas pressure is 0.49 MPa (Luczak et al., 2019)

As shown in Fig. 7, the velocity distribution along the $y = 0$direction of the nozzle-cutting plane is compared with the Particle Image Velocimetry (PIV) experimental data from Luczak. The variable x/D represents the ratio of the radial position within the micronization chamber to the radius, with a fluctuation range of 0-100%. The nozzle trajectory is constrained by the wall, resulting in an arc deflection that creates a grinding zone. Due to the difference in milling pressure boundary conditions, the driving force of jet pressure difference in the LES case is stronger. The peak velocity in the high-speed expansion zone is higher than that of the Luczak case. From a qualitative analysis perspective, the velocity field trends predicted by the LES model agree well with the experimental results. When the number of grid cells is 0.215 million, the peak value in the high-speed expansion region is lower. As x/D approaches 95%, the velocity decay of the coarse grid is also lower than that of the fine grid.

Based on the generalized Richardson extrapolation theory, Roache (1997) proposed a method to evaluate mesh refinement error using GCI. The fundamental concept is to use a second-order method to approximate the results of any grid refinement test against the expected results of a grid doubling. Due to the varying size distribution of non-structural grids, the refinement ratio is calculated based on the number of grids.

$$r = (\frac{N_{k+1}}{N_k})^{1/D} \tag{15}$$

where N is the number of grids, and D is the dimension of the domain area. Based on the constant mesh refinement ratio r and the computational solution of the three sets of meshes, the convergence accuracy p can be directly evaluated.

$$p = ln\left(\frac{f_3 - f_2}{f_2 - f_1}\right) / \ln(r) \tag{16}$$

In the formula, $f_k\ (k = 1,2,3)$ is the numerical solution of three sets of grids from sparse to dense, which can be any physical quantity of interest. In this study, f is taken as the peak velocity v_{max} of the grinding zone.

The Richardson extrapolation method is a high-order estimation method that obtains the continuum value (the value at zero grid spacing) from a series of low-order discrete values (Richardson, 1911). The general form of the numerical solution by series expansion is:

$$f = f_{h=0} + g_1 h + g_2 h^2 + g_3 h^3 + \cdots \tag{17}$$

Among them, h is the grid spacing, and the functions g_1, g_2, g_3 are independent of the grid spacing. $f_{h=0}$ is the continuum value under zero grid spacing. If f is a second-order solution, ignoring the third-order and higher-order terms, $f_{h=0}$ can be derived as:

$$f_{h=0} \cong f_1 + \frac{f_1 - f_2}{r^2 - 1} \tag{18}$$

Eq. (17) is generalized to the case of p −order method and grid ratio r (not necessarily an integer):

$$f_{h=0} \cong f_1 + \frac{f_1 - f_2}{r^p - 1} \tag{19}$$

GCI is a percentage measure of how far the computed value is from the asymptotic value, indicating the error

Table 3 Grid and time dependence of v_{max}

Minimum Grid Size (mm)	N_k	$dt\ (ms)$	v_{max} (m/s)	r	p	ε	GCI (%)	$f_{h=0}$
0.07	1818063	0.01	250.578	1.4	-1.58	0.0101	3.06	252.6
0.15	615147	0.01	248.134			0.0126	2.24	
0.2	214916	0.01	244.998			-	-	
0.15	615147	0.005	248.923			-	-	
0.15	615147	0.05	247.261			-	-	

band away from the asymptotic value. That is, with further grid refinement, the degree of deviation of the solution. When GCI is small, it indicates that the computed value is within the asymptotic range. The definitions of GCI on fine and coarse grids are:

$$GCI_{fine} = F_s \left| \frac{\varepsilon}{r^p - 1} \right| \tag{20}$$

$$GCI_{coarse} = F_s \left| \frac{\varepsilon r^p}{r^p - 1} \right| \tag{21}$$

In the formula: F_s is the safety factor. For the comparison of three sets of grids, take $F_s = 1.25$. The relative error ε is defined as:

$$\varepsilon = \frac{f_2 - f_1}{f_1} \tag{22}$$

By calculating the GCI values on three sets of grids, it can be verified that each numerical solution is within the asymptotic convergence range. The required grid resolution is estimated based on the established expected accuracy level.

$$GCI_{12} / GCI_{23} = r^p \tag{23}$$

According to Equation (22), we verify whether the numerical solution falls within the asymptotic range of convergence.

$$r^p GCI_{23} / GCI_{12} = 0.801 \tag{24}$$

The ratio result is approximately 1, indicating that the numerical solution exhibits good convergence within the asymptotic range. $f_{h=0}$ is 252.6 m/s, and the error band is 1.8%. Significantly, the medium and fine grids demonstrated improved capability in capturing the trends observed in the fluid field's velocity variation. The GCI evaluation results indicate that when the number of grids exceeds 0.615 million, the dependence of peak flow velocity in the milling zone on grid density is low (Table 3). Further refinement of the grid does not significantly affect the evolution of vortex structures inside the micronization chamber. Consequently, the medium grid is selected to study the transient turbulence characteristics during jet milling. Detailed parameters of volume meshing can be found in Table 4.

In this study, we implemented a least-squares cell-based scheme to accurately compute the scalar gradient on the mesh surface. To achieve second-order accuracy in pressure interpolation, we employed a second-order scheme that reconstructs face pressure for each cell using the central difference method. The continuity and momentum equations were discretized using a central bounded difference scheme to minimize numerical diffusion. Pressure-velocity coupling was resolved using the PISO algorithm. To ensure temporal accuracy, we adopted a second-order implicit time differencing method. Time step dependence studies were conducted, and the results are presented in Table 3. For the current study, a time step of 10^{-5} seconds was used.

Table 4 Volumetric mesh parameters

Parameters	Unit	Value
Minimum surface mesh size	mm	0.15
Maximum surface mesh size	mm	0.8
Surface mesh growth rate	-	1.2
Surface mesh size functions	-	Curvature & proximity
Surface mesh curvature normal angle	◦	18
Number of layers	-	3
Boundary layers transition ratio	-	0.272
Boundary layers growth rate	-	1.2
Volume mesh growth rate	-	1.2

4. RESULTS AND DISCUSSION

4.1 Turbulent Transition Behavior

The unidirectional jet is driven by the pressure difference between the working medium distribution chamber and the micronization chamber. Figure 8 shows the time series of the structural evolution of the flow velocity on the nozzle-cutting plane. To better visualize the velocity gradient of the jet flow, the contour map magnifies the nozzle position in the 12 o'clock direction. Due to the persistence of the laminar flow phenomenon, the turbulent outbreak in the chamber is delayed (Patil 2019). After entering the micronization chamber, the high-speed jet expands freely and continuously exchanges momentum with the surrounding static fluid.

A peak-shaped red domain, characterized by peak velocity at its core, forms downstream of each nozzle. Taking the nozzle positioned at the 12 o'clock direction as an example, the peak velocities recorded are 331.35 m/s at 2 ms, 380.56 m/s at 5 ms, 457.56 m/s at 8 ms, 545.44 m/s at 14 ms, 561.38 m/s at 25 ms, 521.30 m/s at 70 ms, 454.14 m/s at 400 ms, and 441.81 m/s at steady state. The micronization chamber and the working medium distribution chamber create a double squeeze effect on the gas flow. The flow velocity in the core region exhibits a trend of initially increasing, followed by a decrease, ultimately approaching a steady state. The evolution of the turbulent structure within the chamber will be discussed in detail below.

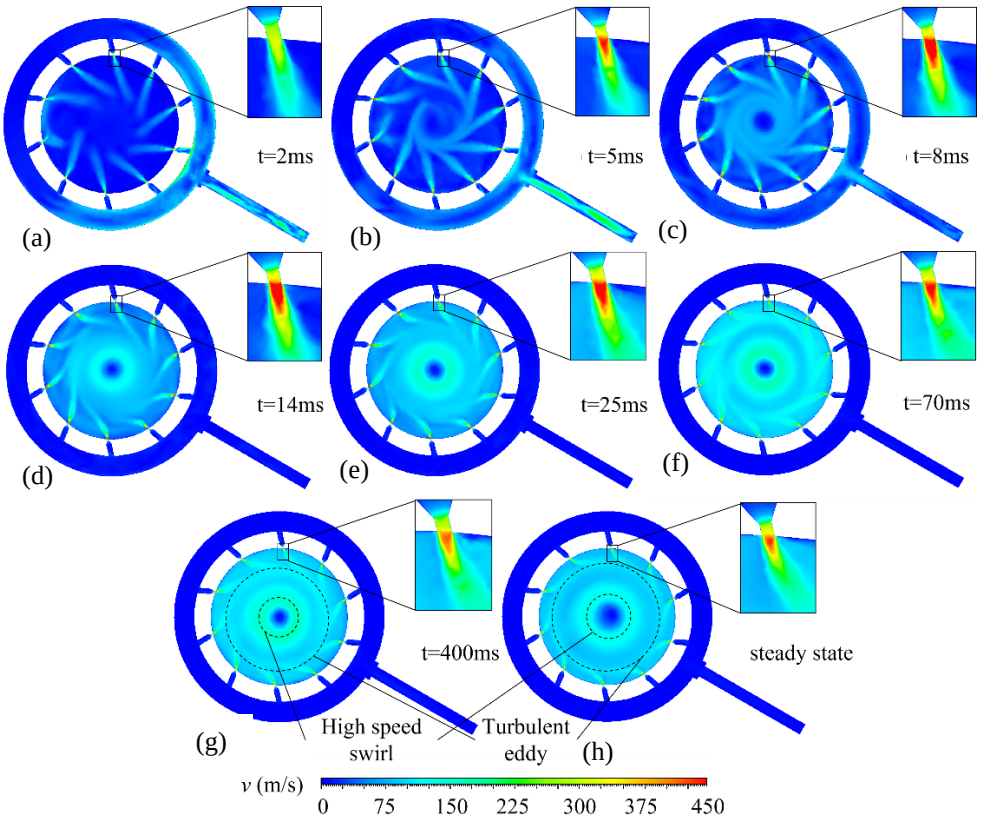

Fig. 8 Time series of fluid velocity field and expansion area of nozzles

At 2 ms, the milling gas flow diffuses bi-directionally within the working medium distribution chamber. A pressure difference forms before and after the nozzle, inducing the initial breakdown of the jet into laminar fluid. As turbulence breaks out, the intensity of the jet along the nozzle direction is diminished by the laminar flow, causing the velocity near the center to drop below 100 m/s. From 5 ms to 8 ms, the diffusion of the milling gas within the working medium distribution chamber intensifies. The jet's penetration force increases, promoting the emergence of a central swirl. Driven by the feeding gas, the tails of multiple high-speed jets deflect and adhere in a clockwise direction, forming a central swirl characterized by high turbulence. The inherent laminar fluid in the micronization chamber is rapidly eroded (Xue et al., 2015). During the interval from 14 ms to 25 ms, the central swirling flow entrains the jet flow, creating a velocity gradient that decays radially from the centre toward the walls. As the simulation time progresses, at 70 ms, due to the limitation of the central swirl on the absorption of high-speed jet, a new turbulent swirl develops around the central swirl. The large-scale expansion of this swirling flow causes a slight increase in pressure within the micronization chamber, while the external milling pressure remains constant. This reduction in pressure difference decreases the driving force of the nozzle. Furthermore, the expansion of the swirl structure toward the walls hinders the impact of the jet. These factors contribute to a reduction in flow velocity in the core region and a decrease in the depth of the red fluid field. The flow velocity evolution structure observed at 400 ms and in the steady state exhibits several similar key characteristics, indicating that a stable swirl structure has formed within the micronization chamber.

4.2 Velocity component

Figures 9 and 10 show the changes in the nozzle-cutting plane's radial and circumferential velocity components. These components create resistance and centrifugal force, which significantly impact particle dispersion. The radial velocity component program overlays the gas motion trajectory in the plane to highlight the influence of radial velocity on streamline contraction and expansion. Like the gas velocity distribution, the radial component forms a peak core downstream of the nozzle. Due to jet expansion, the peak region of radial velocity decreases rapidly in the transverse direction (Xue et al., 2013). For instance, if we take the nozzle positioned at the 12 o'clock direction as an example, the radial components in the core area are -296.53 m/s at 2 ms, -435.28 m/s at 5 ms, -480.21 m/s at 8 ms, -485.63 m/s at 14 ms, -443.72 m/s at 70 ms, and -443.37 m/s at 400 ms. The radial velocity across the entire fluid domain fluctuates between -480 and 160 m/s, with the radial component reaching 0 in the yellow region.

At 2 ms, the clockwise peak of the circumferential velocity appears in the right nozzle throat; the counterclockwise peak appears in the working fluid distribution chamber near the inlet of the milling gas. There is a higher number of irregular spikes in the circumferential velocity at this time, indicating that wall constraints cause the initial motion state of the milling gas to become chaotic. The closed streamline observed in the working fluid distribution chamber results from the WALE model confining the large-scale turbulence. The central swirl structure remains underdeveloped at this stage. As the jet penetration length increases, the gas streamline is affected by the weakening of the radial

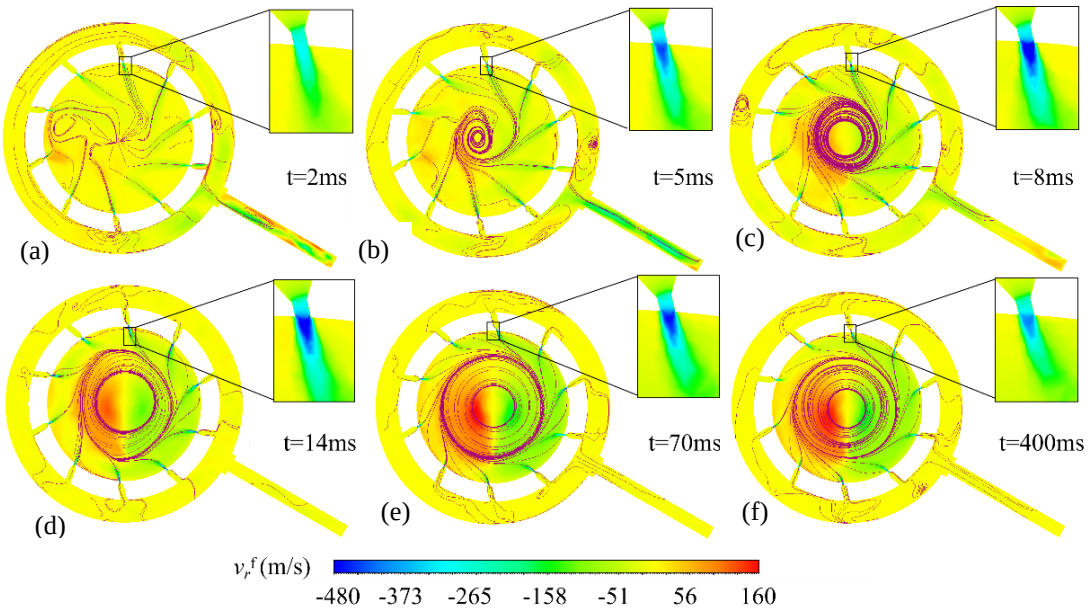

Fig. 9 Time series of radial velocity and streamline distribution

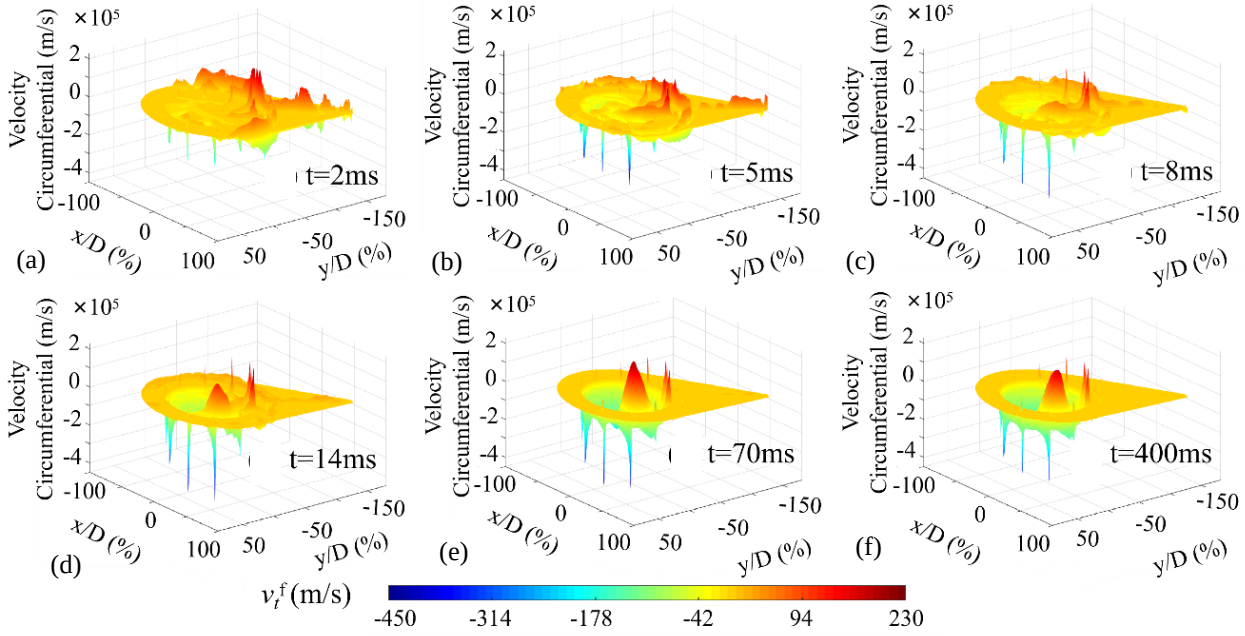

Fig. 10 Time series of gas flow circumferential velocity distribution

component. The streamline creates an axis intersection following a significant deflection at the jet tail. In the direction of 9 to 8 o'clock, small vortices are generated within the micronization chamber by the jet streamline due to interference from feeding gas.

At 5 ms, the formation of continuous jet streamlines fosters swirl germination. The momentum of the edge flow transforms into the central domain. The rapid evolution of the radial and circumferential components causes local oscillation of the swirl streamline. At 8 ms, the circumferential velocity of the nozzle cutting plane shows a distribution trend dominated by the instantaneous needle direction of the edge and assisted by the downstream counterclockwise direction. The radial velocity exhibits a preliminary anti-symmetric distribution: the left red region demonstrates centrifugal ositive velocity, causing particle-wall collisions; the green region on the right represents centripetal negative flow velocity, compelling particles to return to the micronization chamber (Ishihara et al., 2020). The distance between the axle centre and any fixed point on the streamline is reduced, and the spiral streamlines resemble the dense superposition of multiple concentric circles. After 14 ms, once the differential velocity distribution in the working medium distribution chamber disappears, the jet motion tends to be stable. The distribution structure of the radial and circumferential components within the circular region gradually becomes more defined. Driven by the bidirectional forces of the component velocities, concentrated spiral flow oscillates inward and outward, creating a spiral trajectory.

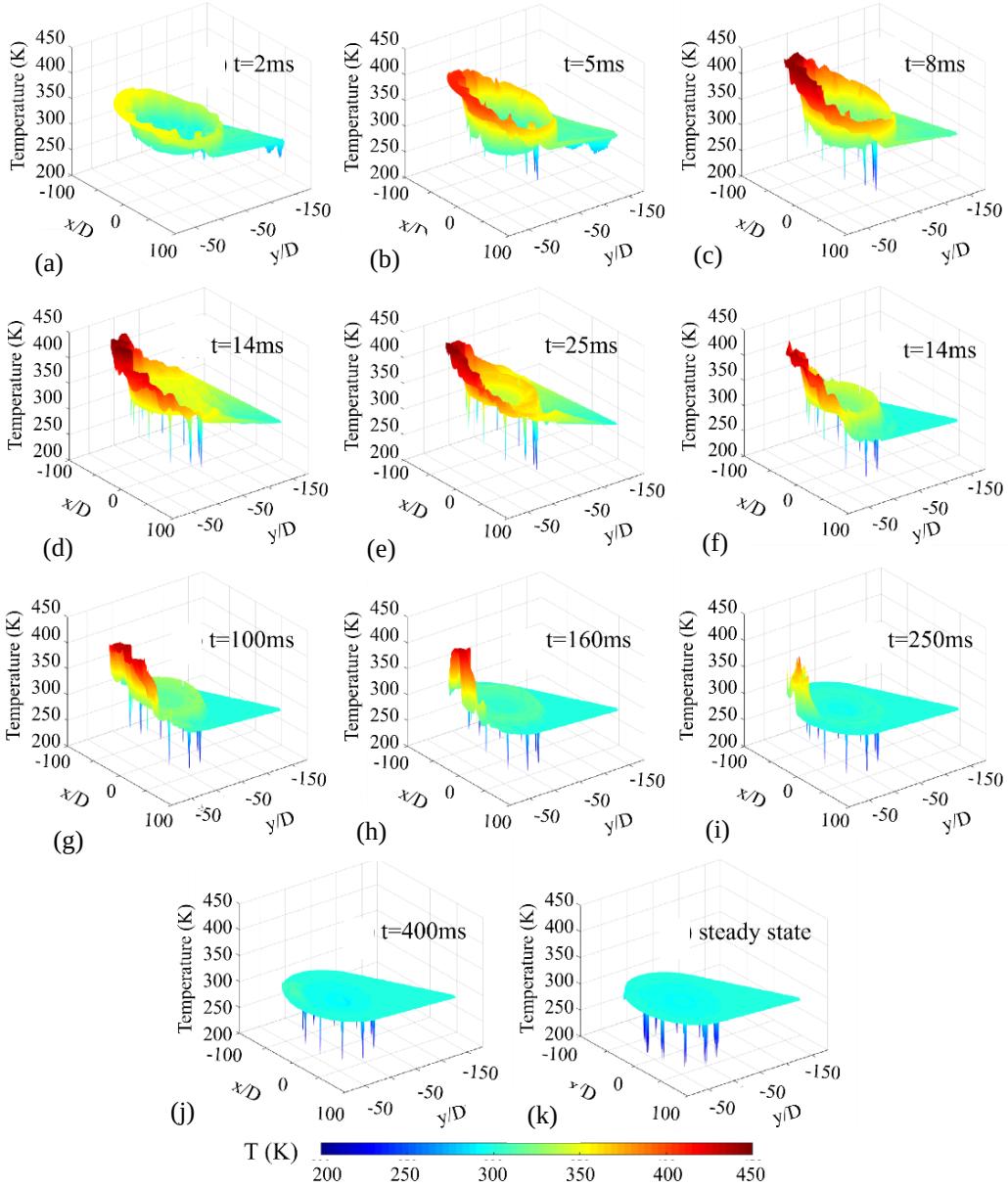

Fig. 11 Time series of gas flow temperature distribution on nozzle cutting plane

4.3 Convective Heat Transfer

Due to the complexity of the fluid field within the chamber, achieving sufficient resolution for dynamic experimental characterization is challenging. It complicates the capture of the heat transfer processes associated with turbulent fluctuations. The simulation accuracy of the jet milling system is highly dependent on the effectiveness of turbulence modelling (Najafiyazdi et al., 2023). Turbulence is characterized by eddy currents with a wide range of length and time scales. The LES model is especially effective in capturing the intricate details of vortices across this broader spectrum of scales (Wu et al., 2000; Boddupalli et al., 2018).

This section presents the time series of the temperature field in the nozzle cutting plane (refer to Fig. 11). Firstly, the high-speed gas, confined and impacted by the chamber wall, generates high turbulent fluctuations in the working medium distribution chamber. It intensifies the convective heat transfer process within the impact zone. Secondly, as analyzed in Fig. 8, the high-speed jet expands freely within the laminar domain. The shear stress generated by momentum exchange drives the formation of swirl structures and enhances the convective heat transfer coefficient at the nozzle throat position. The injection system's energy dissipation increases local heat transfer, causing the gas flow around the wall to heat up.

From 2 ms to 25 ms, the milling gas renders the annular working fluid distribution chamber. Forced convection occurs at the closure, resulting in a differential distribution of the annular density field. Turbulence oscillation promotes the dynamic transfer process of energy. The peak temperature of the impact zone is 391 K at 2 ms, 407 K at 5 ms, 444.41 K at 8 ms, 447.67 K at 14 ms, and 450.34 K at 25 ms. A strong density gradient is formed before and after the nozzle, pushing the compressed gas into the micronization chamber. At 70 ms, the flow velocity in the core region decreases, and the turbulent fluctuation in the working fluid distribution

chamber is limited. Affected by the nozzle position, the temperature presents a stepped distribution in the three-dimensional coordinate system. Between 100 and 250 ms, based on the limitation and compression of the micronization chamber on the gas flow, the trajectory of the milling gas tends to be regular. The temperature peak domain shrinks with time. At 400 ms, the flow trajectory has evolved to a stable state, and the correlation between the density gradient and the coordinates is weakened. The temperature field in the system tends to stabilize, which is consistent with the numerical simulation results solved by the k-epsilon model. Based on this, the results of the unsteady LES model proposed in this paper are essentially correct. A deeper understanding of the jet structure and vortex field evolution mechanisms will help drive the structural optimization of jet milling equipment.

4.4 Coherent Vortex Structure

Coherent structure is a vortex motion that interferes with each other in space and evolves with time. It is crucial for analyzing the momentum exchange and the evolution of swirl topology in wall boundary turbulence (Jiang, 2019). In this work, the Q criterion is applied to visualize the turbulent coherent structure, which is defined as:

$$Q = \frac{1}{2}[\|\Omega\|^2 - \|S\|^2] \tag{25}$$

Among them, $S = 1/2(\nabla u + (\nabla u)^T)$, $\Omega = 1/2(\nabla u - (\nabla u)^T)$ (Severac et al., 2007; Kareem, 2017).

Figure 12 illustrates the coherent vortex structures of the gas flow field in the working medium distribution chamber and micronization chamber at different time points. The coloration represents the Reynolds number. Figure 13 displays the time series of vorticity distribution within the fluid domain. The multi-scale chamber contributes to the development of intricate and disordered turbulent coherent structures during the evolution of swirl topology. This is primarily manifested by the migration and fragmentation of large eddy structures and the formation of large-scale annular swirls.

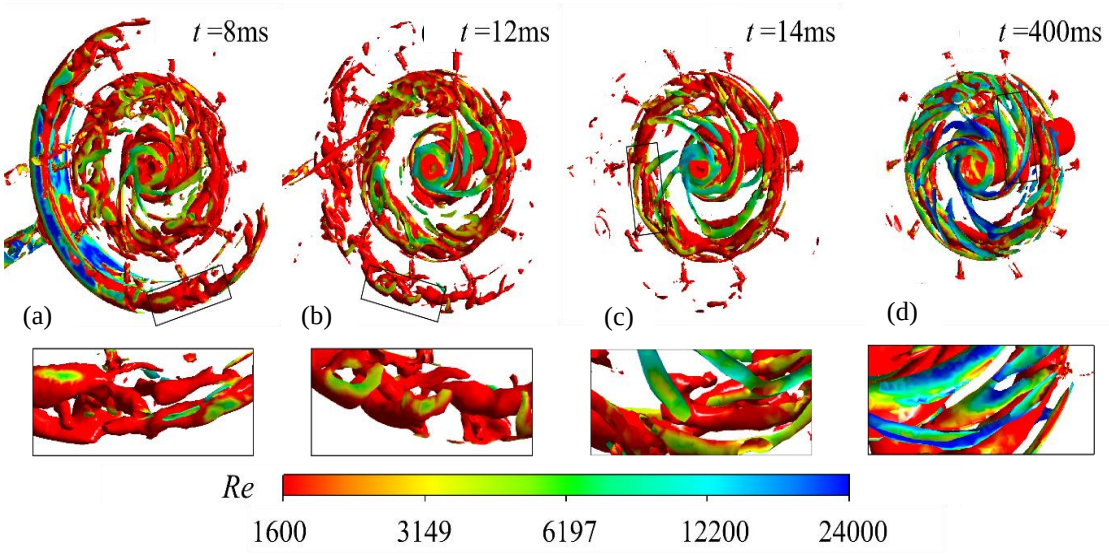

Fig. 12 Time series of coherent structure evolution in micronization chamber

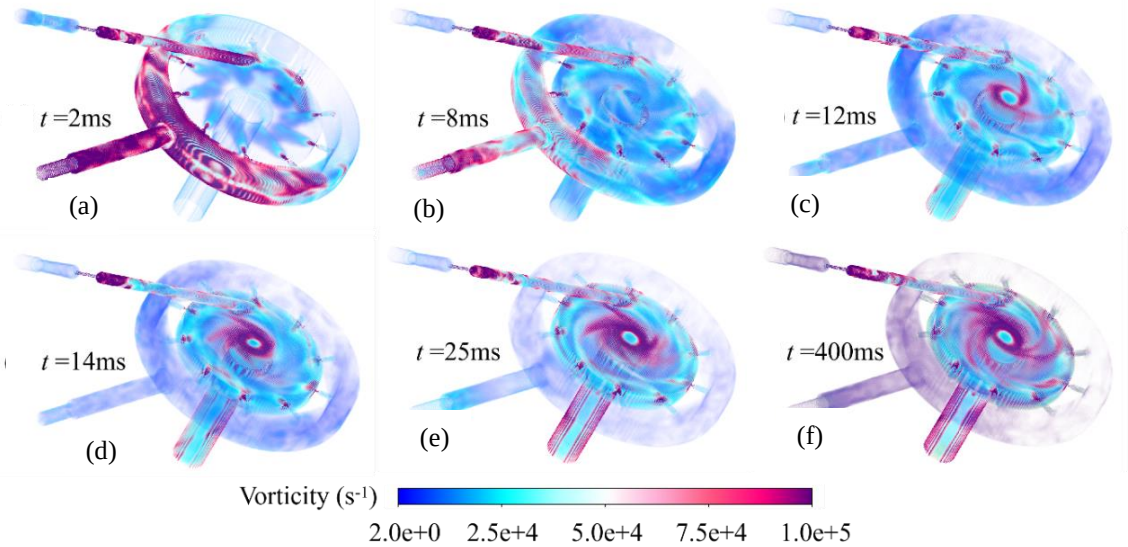

Fig. 13 Vorticity distribution at different times

At 8 ms, the milling gas hits the working medium distribution chamber. The strong turbulent fluctuation causes the Reynolds number of the local wall fluid domain to surge to more than 20,000. The fluid impact under the pressure gradient enhances the stretching of the high vorticity flow in the direction of motion, thus forming a large vortex structure with circumferential extension. The milling gas is compressed and sheared by the laminar flow domain and the wall surface, resulting in unstable transport. Compared to the 2 ms moment, the vorticity in the working fluid distribution chamber experiences a significant reduction in magnitude. This attenuation is due to turbulent dissipation and energy loss of the milling gas during impact. At the rear of the large eddy structure, the corresponding vorticity is only 2. The vorticity attenuation causes the vortex structure at the tail of the gas flow to be unable to be maintained, resulting in discontinuity. In addition, the disordered folding deformation of some large eddy structures may also be related to the strong traction disturbance of the nozzle. The large eddy structure is decomposed into numerous stripe vortices by the spiral absorption of the nozzle. The high energy dissipation generated by the jet breakdown causes the streak vortex to expand laterally. The Coriolis force induces its rapid deflection and distribution along the circumferential direction (Shena & Wang, 2022). The height of the micronization chamber limits the free movement of the gas. The streak vortices moving along the axial direction attract each other and combine into a closed annular large-scale swirl downstream of the chamber. This phenomenon is more significant with the passage of simulation time. Part of the streak vortex upstream of the chamber is distorted. This is caused by the absorption of the stripe vortex by the large-scale swirl structure and the incomplete fusion of the feeding gas. At 12 ms, the rendering degree of the milling gas intensifies. The compressed flow in the working fluid distribution chamber tends to relax. The attenuation of gas velocity leads to the fracture of large eddy structures related to weak compressibility, forming multiple interlaced hairpin vortices (Jiang, 2019). Within the micronization chamber, a dominant large-scale vortex governs the mixing of the jet's coherent structure. This vortex entrains streak vortices, forming a spiral winding structure with closed circulation at its core. After 14 ms, the coherent structure in the working medium distribution chamber essentially declines, and the gas flow tends to be irrotational. The vortex core structure limits the absorption of the jet. Therefore, the fringe vortices distributed upstream of the chamber interfere with each other in the central domain, forming a high Reynolds number swirl in the upper wall domain.

5. CONCLUSIONS

This article employs the WALE subgrid-scale model in the LES method to quantitatively describe the unsteady evolution process of the swirl structure in the spiral jet mill. The analysis covers flow velocity distribution, heat transfer process, and coherent structure, providing theoretical support for numerical simulation of multi-scale strong oxidant preparation. The visualization results reveal that the peak flow velocity in the core area initially increases and then decreases, a behavior attributed to the double-squeezing effect of the wall structure and the fluid. The momentum of the edge flow is converted to the central domain through the traction exerted by the feeding gas and the attenuation of the jet impact. It promoted the germination of the central swirl in the micronization chamber. The trans-scale chamber structure contributes to the intricate and disorderly nature of the turbulent coherent structure during the swirl topology evolution. Multiple strip vortices intertwine and superimpose, forming a large-scale annular swirl. The velocity profile and temperature distribution at 400 ms closely align with the steady-state solution of the k-epsilon model. At this point, the radial and circumferential velocities exhibit regular distributions, and the flow trajectory follows a spiral pattern. During the spiral jet milling process, the jet and high-speed particles strongly impact the wall. Long working hours may cause damage to the equipment, necessitating regular maintenance of the micronization chamber and nozzle.

This article is limited to simulating and predicting the fluid dynamics behavior inside the spiral jet mill. An ideal predictive simulation tool should integrate non-isothermal, compressible, high Mach number fluid flow, interaction between gas-solid two-phase flows, and fracture mechanics of particle collisions to accurately describe the jet milling process. It will facilitate the prediction of the classification mechanism and fracture behavior of particles within the grinding force field. This analysis will be the subject of future communication.

CONFLICT OF INTEREST

The authors declare that they have no known competing financial interests or personal relationships that could have appeared to influence the work reported in this paper.

AUTHORS CONTRIBUTION

Yizhe Yu: software, validation, data analysis, writing—original draft preparation, visualization; **Kaixuan Chen:** software, validation, data curation, writing—original draft preparation; **Deqi Wang:** validation, writing—original draft preparation; **Yang Qin:** validation, visualization; **Jie Liu:** data analysis, visualization.

REFERENCES

Alzwayi, A. S., Paul, M. C., & Navarro-Martinez, S. (2014). Large eddy simulation of transition of free convection flow over an inclined upward facing heated plate. *International Communications in Heat and Mass Transfer, 57*, 330-340. http://doi.org/10.1016/j.icheatmasstransfer.2014.08.009

Bnà, S., Ponzini, R., Cestari, M., Cavazzoni, C., Cottini, C., & Benassi, A. (2020). Investigation of particle dynamics and classification mechanism in a spiral jet mill through computational fluid dynamics and

discrete element methods. *Powder Technology, 364*, 746-773. http://doi.org/10.1016/j.powtec.2020.02.029

Boddupalli, N., Yadav, N. K., & Chandra, L. (2018). The unsteady flow features behind a heliostat in a narrow channel at a high Reynolds number: Experiment and Large Eddy Simulation. *International Journal of Mechanical Sciences, 136*, 424-438. http://doi.org/10.1016/j.ijmecsci.2017.12.048

Bojko, B. T., Gross, M. L., & Jackson, T. L. (2020). Investigating dimensional effects on predicting burning rates of heterogeneous solid propellants. *AIAA Journal, 58*(4), 1724-1732. http://doi.org/10.2514/1.J058631

Brosh, T., Kalman, H., Levy, A., Peyron, I., & Ricard, F. (2014). DEM-CFD simulation of particle comminution in jet-mill. *Powder Technology, 257*, 104-112. http://doi.org/10.1016/j.powtec.2014.02.043

Chen, K. X., Xue, X. C., Yu, Y. G., & Z. Ye, W. (2023). Microflame diffusion properties of AP/HTPB propellant under binder width effects. *Journal of Mechanical Science and Technology, 37*(2), 1037-1046. http://doi.org/10.1007/s12206-023-0142-1

Chen, X. H., Long, Y., Wang, Y. Z., Weng, S. L., & Luan, Y. J. (2021). Large eddy simulation of film cooling from cylindrical holes partially blocked by CaO-MgO-Al_2O_3-SiO_2. *International Communications in Heat and Mass Transfer, 129*. http://doi.org/10.1016/j.icheatmasstransfer.2021.105754

Gross, M. L. & Beckstead, M. W. (2010). Diffusion flame calculations for composite propellants predicting particle-size effects. *Combustion and Flame, 157*(5), 864-873. http://doi.org/10.1016/j.combustflame.2009.09.004

Isert, S., Hedman, T. D., Lucht, R. P. & Son, S. F. (2016). Oxidizer coarse-to-fine ratio effect on microscale flame structure in a bimodal composite propellant. *Combustion and Flame, 163*, 406-413. http://doi.org/10.1016/j.combustflame.2015.10.015

Ishihara, T., Qian, G. W., & Qi, Y. H. (2020). Numerical study of turbulent flow fields in urban areas using modified k - ε model and large eddy simulation. *Journal of Wind Engineering and Industrial Aerodynamics, 206*. http://doi.org/10.1016/j.jweia.2020.104333

Jafari, A., Zamankhan, P., Mousavi, S. M., & Pietarinen, K. (2008). Modeling and CFD simulation of flow behavior and dispersivity through randomly packed bed reactors. *Chemical Engineering Journal, 144*(3), 476-482. http://doi.org/10.1016/j.cej.2008.07.033

Jiang, X. Y. (2019). Revisiting coherent structures in low-speed turbulent boundary layers. *Applied Mathematics and Mechanics-English Edition, 40*(2), 261-272. http://doi.org/10.1007/s10483-019-2445-8

Kareem, W. A. (2017). Anisotropic complex diffusion filtering for comparison of the vortex identification methods in homogeneous turbulence. *International Journal of Mechanical Sciences, 134*, 291-305. http://doi.org/10.1016/j.ijmecsci.2017.10.023

Kumar, T., & Jackson, T. L. (2021). Three-dimensional thermo-mechanical simulations of heterogeneous solid propellants. *Combustion and Flame, 233*. http://doi.org/10.1016/j.combustflame.2021.111590

Luczak, B., Müller, R., Kessel, C., Ulbricht, M., & Schultz, H. J. (2019). Visualization of flow conditions inside spiral jet mills with different nozzle numbers- Analysis of unloaded and loaded mills and correlation with grinding performance. *Powder Technology, 342*, 108-117. http://doi.org/10.1016/j.powtec.2018.09.078

Nagendra, K., Ingole, M. & Periyapatna, R. A. (2019). Experimental studies on low pressure deflagration limit of ammonium perchlorate with additives. *Combustion and Flame, 207*, 356-367. http://doi.org/10.1016/j.combustflame.2019.06.011

Najafiyazdi, M., Mongeau, L., & Nadarajah, S. (2023). Large eddy simulation on unstructured grids using explicit differential filtering: A case study of Taylor-Green vortex. *Journal of Computational Physics, 476*. http://doi.org/10.1016/j.jcp.2022.111833

Patil, R. H. (2019). Fluid flow and heat transfer analogy for laminar and turbulent flow inside spiral tubes. *International Journal of Thermal Sciences, 139*, 362-375. http://doi.org/10.1016/j.ijthermalsci.2019.01.036

Rajeswari, M. S. R., Azizli, K. A. M., Hashim, S. F. S., Abdullah, M. K., Mujeebu, M. A., & Abdullah, M. Z. (2011). CFD simulation and experimental analysis of flow dynamics and grinding performance of opposed fluidized bed air jet mill. *International Journal of Mineral Processing, 98*(1-2), 94-105. http://doi.org/10.1016/j.minpro.2010.10.012

Richardson, L. F. (1911). The approximate arithmetical solution by finite differences of physical problems involving differential equations, with an application to the stresses in a masonry dam. *Philosophical Transactions of the Royal Society of London, 210***,** 307-357. http://doi.org/10.2307/90994

Roache, P. J. (1997). Quantification of uncertainty in computational fluid dynamics. *Annual Review of Fluid Mechanics, 29*(1), 123-160. https://doi.org/10.1146/annurev.fluid.29.1.123

Rodnianski, V., Krakauer, N., Darwesh, K., Levy, A., Kalman, H., Peyron, I., & Ricard, F. (2013). Aerodynamic classification in a spiral jet mill. *Powder Technology, 243*, 110-119. http://doi.org/10.1016/j.powtec.2013.03.018

Sabia, C., Casalini, T., Cornolti, L., Spaggiari, M., Frigerio, G., Martinoli, L., Martinoli, A., Buffo, A., Marchisio, D. L., & Barbato, M. C. (2022). A novel uncoupled quasi-3D Euler-Euler model to study the spiral jet mill micronization of pharmaceutical

substances at process scale: model development and validation. *Powder Technology*, *405*. http://doi.org/10.1016/j.powtec.2022.117573

Sabia, C., Frigerio, G., Casalini, T., Cornolti, L., Martinoli, L., Buffo, A., Marchisio, D. L., & Barbato, M. C. (2021). A detailed CFD analysis of flow patterns and single-phase velocity variations in spiral jet mills affected by caking phenomena. *Chemical Engineering Research & Design*, *174*, 234-253. http://doi.org/10.1016/j.cherd.2021.07.031

Scott, L., Borissova, A., Burns, A., & Ghadiri, M. (2021a). *Analysis of hold-up and grinding pressure in a spiral jet mill using CFD-DEM*. The European Physical Journal Conferences, 249, 12004. http://doi.org/10.1051/epjconf/202124912004

Scott, L., Borissova, A., Burns, A., & Ghadiri, M. (2021b). Influence of holdup on gas and particle flow patterns in a spiral jet mill. *Powder Technology*, *377*, 233-243. http://doi.org/10.1016/j.powtec.2020.08.099

Scott, L., Borissova, A., Burns, A., & Ghadiri, M. (2021c). Effect of grinding nozzles pressure on particle and fluid flow patterns in a spiral jet mill. *Powder Technology*, *394*, 439-447. http://doi.org/10.1016/j.powtec.2021.07.090

Severac, E., Poncet, S., Serre, E., & Chauve, M. P. (2007). Large eddy simulation and measurements of turbulent enclosed rotor-stator flows. *Physics of Fluids*, *19*(8). http://doi.org/10.1063/1.2759530

Shen, W. J., & Wang, S. F. (2022). Large eddy simulation of turbulent flow and heat transfer in a turbine disc cavity with impellers. *International Communications in Heat and Mass Transfer*, *139*. http://doi.org/10.1016/j.icheatmasstransfer.2022.106463

Silvester, S. A., Lowndes, I. S., Kingman, S. W., & Arroussi, A. (2007). Improved dust capture methods for crushing plant. *Applied Mathematical Modelling*, *31*(2), 311-331. http://doi.org/10.1016/j.apm.2005.11.005

Tanaka, M., & Yanase, S. (2008). The structure and dynamics of coherent vortex tubes in the zero-absolute-vorticity state. *Journal of Turbulence*, *9*(44), 1-32. http://doi.org/10.1080/14685240802562038

Versteeg, H., & Malalasekera, W. (1995). *An introduction to computational fluid dynamics: The Finite volume method*. 2nd edition. PEARSON Prentice Hall.

Wang, M. Y., Lu, X. G., Yang, C. W., Zhao, S. F., & Zhang, Y. F. (2023). Control of separated flow transition over a highly loaded compressor blade via dynamic surface deformation. *International Journal of Mechanical Sciences*, *241*. http://doi.org/10.1016/j.ijmecsci.2022.107980

Wu, X. H., & Squires, K. D. (2000). Prediction and investigation of the turbulent flow over a rotating disk. *Journal of Fluid Mechanics*, *418*, 231-264. http://doi.org/10.1017/s0022112000001117

Wu, Y. J., Yu, S. F., & Zuo, L. (2019). Large eddy simulation analysis of the heat transfer enhancement using self-oscillating fluidic oscillators. International *Journal of Heat and Mass Transfer*, *131*, 463-471. http://doi.org/10.1016/j.ijheatmasstransfer.2018.11.070

Xue, X. C., Yu, Y. G., & Zhang, Q. (2013). Study on expansion characteristic of twin combustion gas jets in five-stage cylindrical stepped-wall observation chamber. *Flow Turbulence and Combustion*, *91*(1), 139-155. http://doi.org/10.1007/s10494-013-9461-0

Xue, X. C., Yu, Y. G., & Zhang, Q. (2015). Study on the influences of interaction behaviors between multiple combustion-gas jets on expansion characteristics of Taylor cavities. *Acta Mechanica Sinica*, *31*(5), 720-731. http://doi.org/10.1007/s10409-015-0421-x